PNAS RESEARCH ARTICLE | CELL BIOLOGY OPEN ACCESS

In situ architecture of the lipid transport protein VPS13C at ER–lysosome membrane contacts

Shujun Cai[a,b,c,d,e], Yumei Wu[a,b,c,d,e], Andrés Guillén-Samander[a,b,c,d,e], William Hancock-Cerutti[a,b,c,d,e], Jun Liu[b,1], and Pietro De Camilli[a,b,c,d,e,1]

Edited by James Hurley, University of California Berkeley, Berkeley, CA; received March 2, 2022; accepted June 2, 2022

VPS13 is a eukaryotic lipid transport protein localized at membrane contact sites. Previous studies suggested that it may transfer lipids between adjacent bilayers by a bridge-like mechanism. Direct evidence for this hypothesis from a full-length structure and from electron microscopy (EM) studies in situ is still missing, however. Here, we have capitalized on AlphaFold predictions to complement the structural information already available about VPS13 and to generate a full-length model of human VPS13C, the Parkinson's disease–linked VPS13 paralog localized at contacts between the endoplasmic reticulum (ER) and endo/lysosomes. Such a model predicts an ∼30-nm rod with a hydrophobic groove that extends throughout its length. We further investigated whether such a structure can be observed in situ at ER–endo/lysosome contacts. To this aim, we combined genetic approaches with cryo-focused ion beam (cryo-FIB) milling and cryo–electron tomography (cryo-ET) to examine HeLa cells overexpressing this protein (either full length or with an internal truncation) along with VAP, its anchoring binding partner at the ER. Using these methods, we identified rod-like densities that span the space separating the two adjacent membranes and that match the predicted structures of either full-length VPS13C or its shorter truncated mutant, thus providing in situ evidence for a bridge model of VPS13 in lipid transport.

lipid-transfer protein | membrane contact sites | VPS13 | cryo-electron tomography

Significance

Lipid transport proteins mediate lipid traffic between subcellular organelles by shielding them in hydrophobic cavities as they travel through the cytosol. Many such proteins are localized at membrane contacts, where they ferry lipids by protein modules that shuttle between the two membranes. However, a bridge-like mechanism has been suggested recently for proteins of the VPS13-ATG2 family. Here, we provide strong support for this model by visualizing a member of this family, VPS13C, in its natural context within cells, contacts between the endoplasmic reticulum (ER) and lysosomes. Its in situ architecture at these contacts is consistent with its functioning as a bridge that allows lipids to slide between closely apposed bilayers along a hydrophobic groove that runs along its entire length.

Communication between subcellular membranous organelles mediated by direct contacts not leading to their fusion plays a critical role in the physiology of eukaryotic cells and is an important complement to interorganelle communication mediated by vesicular transport. The endoplasmic reticulum (ER), in particular, establishes direct contacts with all other membranous organelles of the cell (1). One of the functions of such contacts is to mediate lipid transfer between the two closely apposed membranes via proteins that contain lipid transport modules and also act as direct or indirect tethers between them (2–4). Until few years ago, lipid transfer proteins acting at membrane contact sites in eukaryotic cells were thought to act exclusively by a shuttle mechanism, that is, via modules that harbor one or few lipids and shuttle back and forth between the two participating membranes (5). However, recent studies have also suggested the occurrence of proteins that provide hydrophobic bridges along which lipids can move directly from one bilayer to another to achieve bulk lipid transport (5, 6).

The founding member of this class of protein is VPS13, a protein first identified in yeast by genetic screens for membrane traffic proteins (7–9). Subsequently, VPS13 was putatively linked to lipid transport because of the identification of VPS13 dominant mutations as suppressors of the deficiency of ERMES (ER–mitochondria encounter structure), a protein complex that mediates lipid transport between the ER and mitochondria in yeast (10, 11). The human genome comprises four VPS13 proteins, referred to as VPS13A, VPS13B, VPS13C, and VPS13D, which have different localizations at membrane contact sites and whose mutations result in neurodevelopmental defects or neurodegenerative conditions (12–15). A role of VPS13 family proteins in lipid transport, and more specifically at membrane contact sites, has now been supported by genetic, biochemical, imaging, and structural studies (6, 10, 11, 16–21). Fragments of VPS13 were shown to contain multiple lipids and to transfer lipids between artificial liposomes (17). Crystallographic studies of the N-terminal region of VPS13 of *Chaetomium thermophilum* revealed a hydrophobic cavity (17), which cryo-EM studies of a longer rod-like fragment of the same protein subsequently suggested to continue as a hydrophobic groove along the entire length of the fragment (19). Moreover, binding sites for the ER and for other organelles have been identified in the N-terminal and C-terminal regions of several VPS13 family members, respectively (17, 18, 20–22). Together, these results have suggested a bridge model of lipid transport ideally suited for the bulk delivery of lipids and in line with some of the proposed functions of VPS13 family members in membrane expansion (6). The identification of

Author affiliations: [a]Department of Neuroscience, Yale University School of Medicine, New Haven, CT 06510; [b]Department of Cell Biology, Yale University School of Medicine, New Haven, CT 06510; [c]HHMI, Yale University School of Medicine, New Haven, CT 06510; [d]Program in Cellular Neuroscience, Neurodegeneration and Repair, Yale University School of Medicine, New Haven, CT 06510; and [e]Aligning Science Across Parkinson's (ASAP) Collaborative Research Network, Chevy Chase, MD 20815

Author contributions: S.C. and P.D.C. designed research; S.C., Y.W., and A.G.-S. performed research; W.H.-C. contributed new reagents/analytic tools; S.C., P.D.C., and J.L. analyzed data; and S.C., J.L., and P.D.C. wrote the paper.

The authors declare no competing interest.

This article is a PNAS Direct Submission.

[1]To whom correspondence may be addressed. Email: pietro.decamilli@yale.edu, or jliu@yale.edu.

This article contains supporting information online at http://www.pnas.org/lookup/suppl/doi:10.1073/pnas.2203769119/-/DCSupplemental.

Published July 13, 2022.

regions of amino acid similarity and of predicted structural similarities between VPS13 and the autophagy factor ATG2 had suggested a similar function of ATG2 (17, 23, 24).

Despite these studies, direct evidence for an arrangement of VPS13–ATG2 family proteins in situ that would support a bridge model of lipid transport is still missing. The goal of this study was to fill this gap by combining cryo-focused ion beam (cryo-FIB) milling and cryo-electron tomography (cryo-ET) imaging, a recently developed method that allows us to resolve the in situ structure of proteins of interest at subnanometer resolution (25–27). To this end, we focused on VPS13C, the VPS13 isoform that is localized at ER–late endosome/lysosome (endo/lysosome) contact sites. VPS13C binds the ER via an FFAT motif-dependent interaction with the ER protein VAP and endo/lysosomal membranes via an interaction with Rab7 (17). Overexpression of VPS13C and VAP results in the extensive formation or ER–endo/lysosome contacts, thus facilitating their identification. Our cryo-ET analysis of cell cryo-lamellae generated by cryo-FIB milling provides in situ structural evidence to support the bridge model of lipid transport and also suggests a dynamic interaction of VPS13C with the ER bilayer. VPS13C loss of function results in lysosomal dysfunction at the cellular level (21) and causes familial Parkinson's disease in human patients (14). Moreover, as dysfunction of other VPS13 family also results in neurological diseases (28), a better understanding of in situ architecture VPS13C has implications for both biology and medicine.

Results

Structure of VPS13C as Predicted by AlphaFold. As a premise to the identification of VPS13C by cryo-ET, we took advantage of AlphaFold v2.0 to gain insight into its full-length atomic structure (29). Human VPS13C isoform 1 comprises 3,753 amino acids (a.a.) (Fig. 1A). Since predictions of amino acid sequences longer than 2,000 a.a. by current AlphaFold algorithms are inaccurate, we predicted the structure of three segments of the protein, each one containing a ∼600-a.a. overlap with the adjacent segment, and then aligned them to generate a full-length structure (Fig. 1*B* and *SI Appendix*, Fig. S1 and Movie S1). This structure is represented by a 29.3-nm-long rod whose backbone is a narrow, twisted β-sheet running along its entire length. The β-sheet, which is flanked by α-helices and disordered loops, forms the floor of a hydrophobic groove that extends throughout the rod (Fig. 1 *C* and *D* and Movie S2) and thus could mediate the sliding of lipids from one end to the other end of the protein. The presence of this groove is clearly visible in a view perpendicular to the axis of the rod (Fig. 1*C*), where the groove appears as a tubular cavity given the twisting of the rod. One of the disordered loops surrounding the rod contains the FFAT consensus for binding to VAP and, accordingly, the AlphaFold Multimer algorithm (30) assigns to this loops such interaction (Fig. 1*B* and Movie S1). A region of VPS13 downstream to the so-called VAB domain (Fig. 1*A*), which had previously been described as the APT-1 domain (Fig. 1*A*), comprises the C-terminal portion of the twisted long β-sheet and is directly continuous with the portion of this sheet preceding the VAB domain, so that VAB domain represents an outpocketing of the rod (Fig. 1 *B* and *E*). The β-sheet portion of the APT-1 domain is in turn interrupted by a smaller outpocketing of about 67 a.a., which has sequence and fold similarities to WWE domains (Fig. 1*F* and *SI Appendix*, Fig. S2) (31). This small domain, not previously described in VPS13, is also present in VPS13A (but not VPS13B and VPS13D) and in several VPS13 proteins across evolution. The AlphaFold-predicted shape of the N-terminal ∼330 a.a. of the protein, which comprise the so-called chorein_N motif (∼a.a. 1–120), is in good agreement with the fold of this region from *C. thermophilum* as determined by crystallography, although it is somewhat wider (17). Likewise, the AlphaFold model generally agrees with the cryo-EM structure of the first 1,390 a.a. of VPS13 from *C. thermophilum*, although with a slightly tighter twisting. The VAB domain, which contains six repeats of a module entirely composed of β-sheets (18), and whose crystal structure was recently reported (32), forms an arc structure that probably corresponds to the loop structure previously observed in low-resolution negative staining EM images of yeast VPS13 (16) (Fig. 1*E*). In the AlphaFold-predicted structure, the arc is arranged in a plane roughly perpendicular to the axis of rod, while in the De et al. (16) study, several orientations of arc relative to the rod were reported. Thus, a flexible connection of this region relative to the rod with the possibility of large-scale rotations had been suggested, consistent with the AlphaFold full-length structure. Finally, AlphaFold confirms a C-terminal PH domain preceded by a bundle of four α-helices similar to the C-terminal region of ATG2 (ATG2_C), a region that we had previously called DH-L because of a distant similarity to DH domains (Fig. 1G). Having defined the predicted structure of VPS13C, we set out to build on this information to explore the presence of structures that fit these predictions and their arrangement at membrane contact sites in intact cells.

A Cellular Model for in Situ Analysis of VPS13C-Mediated Contacts. To locate VPS13C-mediated membrane contacts for high-resolution cryo-ET imaging, we first developed a cellular system enriched in such contacts. Overexpression of VPS13C^Halo [tagged at a site found to preserve yeast Vps13 function (11)] and GFP-VAP (VAP-B) with or without Rab7 (possibly because Rab7 is not present at limiting concentration) is sufficient to produce a massive expansion of the normally occurring ER to endo/lysosome contacts (as represented schematically in Fig. 2*A*), resulting in endo/lysosomes completely surrounded by ER cisterns, as shown by fluorescence microscopy (17, 21) (Fig. 2*B*) and electron microscopy (Fig. 2*C*). Frequently this ER is "thin" ER (i.e., ER virtually devoid of a lumen so that the two opposite membranes of the cisterns are in tight apposition to each other, as often observed at contact sites of the ER with other membranes) (33, 34). Endo/lysosomes completely surrounded by ER can also be observed upon overexpression of other proteins that act as tethers between these two organelles (35, 36). One of them is PDZD8, which has an N-terminal transmembrane region anchored in the ER, binds Rab7 on endo/lysosomes, and transports lipids via an SMP domain. Interestingly, coexpression of VPS13C and PDZD8 shows that the two proteins segregate to distinct domains within the contact area between the two organelles (Fig. 2*D*). Furthermore, correlative fluorescence microscopy and focused ion beam scanning electron microscopy (FIB-SEM) not only confirmed that VPS13C and PDZD8 enriched sites corresponded to contacts between endo/lysosomes and the ER but also revealed a striking difference in the distance between the two organelles at the two domains (Fig. 2 *E*, *E'*, and *F* and Movie S3). Although the resolution of FIB-SEM did not allow a precise measurement of such distances, the intermembrane space at PDZD8-positive sites was ∼15 nm, consistent with the distance described previously (35). At VPS13C-positive sites the distance between the two membranes was much greater (Fig. 2 *E*, *E'*, and *F*). The concentration of overexpressed VPS13C at extended

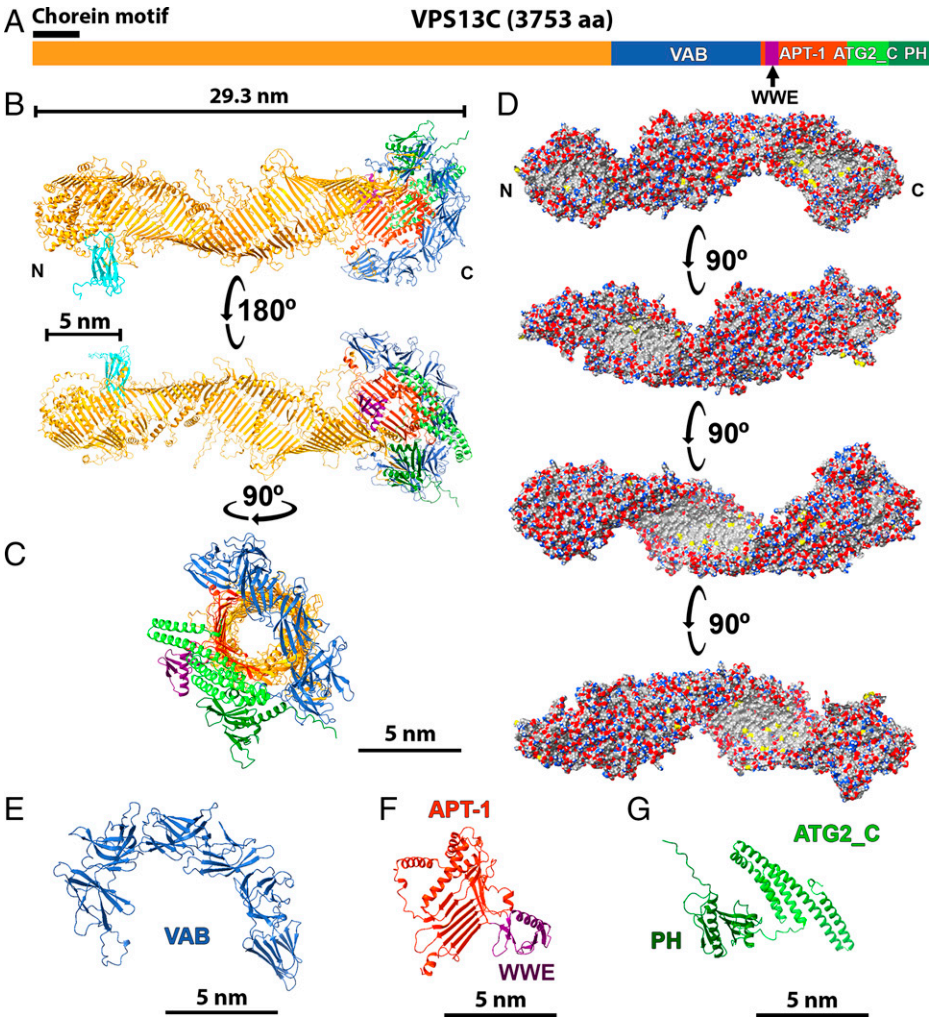

Fig. 1. Structure of VPS13C and its binding partners as predicted from AlphaFold. (*A*) Schematic cartoon of the domain architecture of human VPS13C. (*B* and *C*) Predicted structure of full-length VPS13C in two perpendicular views. The color scheme is consistent with the one shown in panel *A*. The MSP domain of VAPA bound to VPS13C is also shown (in cyan) in field *B*. The groove that runs along the entire protein appears as a tunnel due to the twisting of the elongated β-sheet. (*D*) Surface representations of the protein (90° rotation interval) showing carbon atoms in gray (hydrophobic surfaces), oxygens in red (negative charges), nitrogens in blue (positive charges), and sulfur in yellow. Note the presence of a continuous hydrophobic groove (gray) along the protein. For clarity of presentation, some α-helices and disordered loops are not shown. (*E–G*) Enlarged views of the individual C-terminal domains of the protein. The APT-1 domain forms the C-terminal region of the elongated β-sheet that represents the core of the protein.

ER–endo/lysosome contacts suggested that VPS13C- and VAP-overexpressing cells represent an optimal cellular system to analyze VPS13C-mediated membrane contacts at high resolution by a combination of cryo-FIB milling and cryo-ET imaging.

VPS13C-Mediated Membrane Contacts as Visualized with Cryo-ET. A schematic cartoon of the flow of work to analyze membrane contact sites mediated by VPS13C is shown in Fig. 2*G*. Cells were grown on a gold mesh EM grid, cotransfected with VPS13C^Halo and GFP-VAP-B, and examined by live fluorescence microscopy to identify a cell coexpressing both proteins, where vesicular structures surrounded by both Halo and GFP fluorescence (expected to represent expanded ER–endo/lysosome contacts) could be observed (Fig. 2*B*). The grid was then plunge-frozen, and the selected cell was processed by cryo-FIB milling to generate a ∼150-nm-thick cryo-lamellae to be analyzed by Cryo-ET (Fig. 2*G*). As a negative control, cryo-ET was performed on cells expressing VPS13C^Halo alone, GFP-VAP alone, or neither protein (wild-type cells).

Abundant presence of endo/lysosomes nearly completely surrounded by ER were observed in cryo-lamellae of cells co-overexpressing VPS13C and VAP-B (Fig. 3 *A* and *A*′) but not in the cryo-lamellae of control cells (Fig. 3 *B–D* and *F–H*). At the massive contacts observed in VPS13C- and VAP-B-expressing cells, the distance between the two membranes was relatively uniform (Fig. 3 *A* and *E* and *SI Appendix*, Fig. S3A). A violin plot of membrane spacing measured at multiple sites around different endo/lysosomes shows a peak at ∼33.5 nm (Fig. 4*C*). The same massive ER wrapping (with a similar width of the intermembrane space) was also occasionally observed around organelles enclosed by a double membrane, raising the possibility that they may represent amphisomes (*SI Appendix*, Fig. S3*A*).

Rod-Shaped Bridges at ER–Endo/Lysosome Contacts. Inspection in cryo-electron tomograms of the space between the ER and endo/lysosomes in VPS13C- and VAP-B-overexpressing cells revealed abundant rod-shaped densities about 30 nm in length that bridged the two membranes and were perpendicular to them (Fig. 4 *A*, *A*′, and *D*, Movie S4 and more examples in *SI Appendix*, Fig. S4). The crowding of these rods in the intermembrane space was consistent with the intensity of the fluorescent signal observed in cells from which these tomograms were obtained. In cells expressing only VPS13C^Halo, where VPS13C accumulates on the entire surface of endo/lysosomes

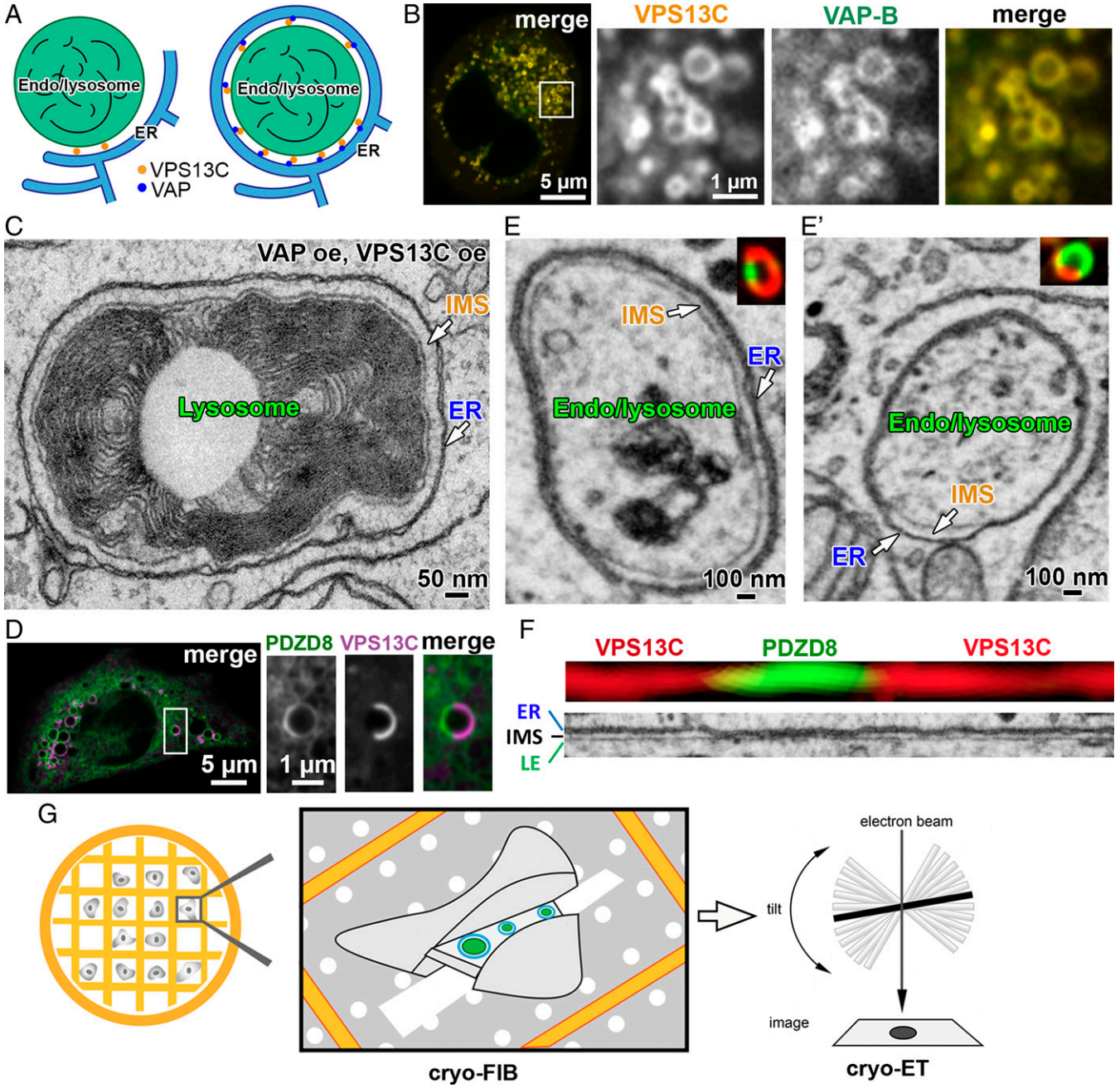

Fig. 2. Experimental system used to visualize VPS13C in situ with cryo-ET. (*A*) Cartoons showing VPS13C-mediated ER–endo/lysosome contacts in wild-type cells (*Left*) and in cell overexpressing VPS13C and VAP-B (*Right*). (*B*) *Left*: "merged" confocal microscopy *z*-slice image of a HeLa cell overexpressing VPS13C^Halo and GFP-VAP. The region enclosed by a box is shown at fivefold enlargement in the split and merged channels at *Right*. The majority of VPS13C^Halo-positive endo/lysosomes are also positive for the ER protein VAP, demonstrating enwrapping by ER. (*C*) Electron micrograph of a lysosome completely surrounded by ER (thin ER) from a COS-7 cell–overexpressing VPS13C and VAP-B. IMS: the inner-membrane space between the ER and the lysosome membrane. (*D*) *Left*: "merged" confocal microscopy *z*-slice image of a Cos-7 cell overexpressing VPS13C^Halo and PDZD8-EGFP. The region enclosed by a box is shown at higher magnification in the split and merged channels at *Right*. (*E* and *E'*) Correlative fluorescence (*Insets*) and FIB-SEM images (large fields) of endo/lysosomes from Cos-7 cells overexpressing VPS13C^halo (red) and PDZD8-EGFP (green). VPS13C (red) and PDZD8 (green) segregate to distinct domains within the contact area between ER (thin ER) and endo/lysosomes. The space between the two organelles is much wider at the contacts where VPS13C is localized. (*F*) Linearized membrane contacts from the same endo/lysosome of panel *E* (processed with Fiji Kymograph) showing the difference in width of the IMS at VPS13C- and PDZD8-positive sites. LE = late endosome/lysosome. (*G*) Cryo-ET workflow. Cells seeded on EM grids were first examined by live confocal microscopy to locate cells overexpressing VPS13C and VAP. Then grids were plunge frozen to maintain the life-like state of cells. ~150-nm-thick cryo-lamellae were generated by cryo-FIB and imaged with cryo-ET.

but does not induce massive ER–endo/lysosome contacts (17) due to the limited amount of endogenous VAP, no such rods were clearly observed (Fig. 3 *B* and *F*). Most likely, in these cells VPS13C is positioned in different orientations, including an orientation parallel to the endo/lysosomal membrane, which would make its detection by cryo-ET very challenging.

To verify that the 30-nm-long rods represent VPS13C molecules, we examined cells expressing a truncated form of VPS13C where a portion of the lipid transfer channel (a.a. 1,235–1,748) had been removed (Fig. 4*B* and *SI Appendix*, Fig. S5 and Movie S5). AlphaFold predictions suggested a length of this construct ~5 nm shorter than full-length VPS13C (Fig. 4*I* and *SI Appendix*, Fig. S1). Accordingly, we found that VPS13C Δ1,235–1,748 rods between ER and endo/lysosomes were ~24 nm long (Fig. 4*E*) and that the intermembrane space was ~5 nm shorter (i.e., 28.5 nm) than the one mediated by

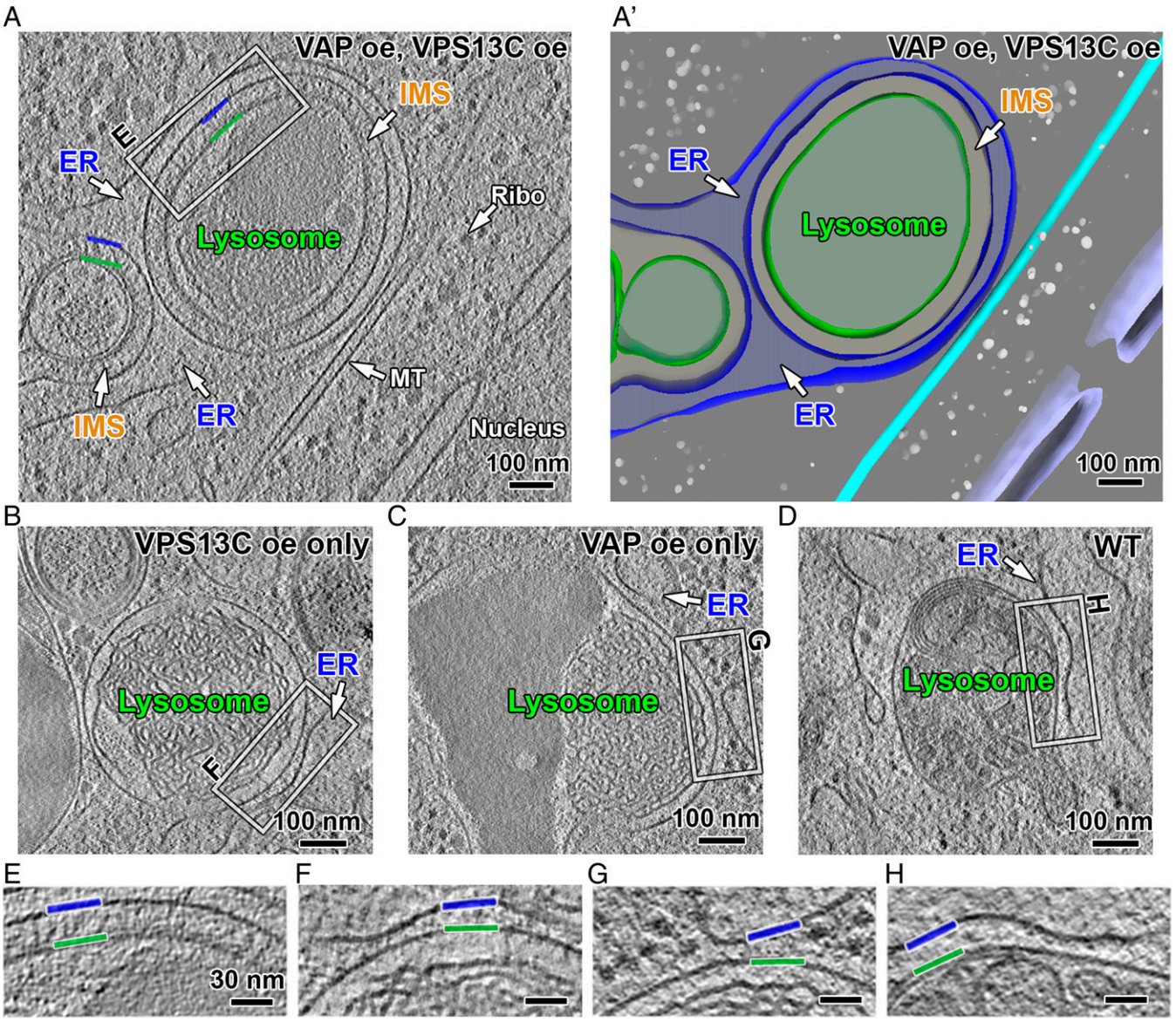

Fig. 3. VPS13C-mediated membrane contact sites. (*A*) Cryo-tomographic slice (1 nm thick) showing VPS13C-mediated membrane contacts between lysosomes and ER in VPS13C and VAP-B co-overexpressing HeLa cell. IMS: inner-membrane space between the ER and the lysosome membrane. (*A'*) 3D view of the tomogram shown in panel *A*. Gray sphere, ribosome; cyan tube, mitochondria; purple, nuclear envelope. (*B–D*) Negative controls showing contacts between lysosomes and ER in cells without VPS13C and VAP co-overexpression. (*E–H*) Enlarged views (twofold) of the region boxed in panels *A–D* showing ER–lysosome contacts. Blue and green lines: ER and lysosome membrane, respectively. oe: over-expression, MT: microtubule, WT: wild type.

full-length VPS13C (Fig. 4*C*). Taken together, our comparative cryo-ET analyses of full-length VPS13C and VPS13C Δ1,235–1,748 indicate that rod-shaped VPS13C bridges two membranes in situ.

To gain further insight into the characteristics of the rod-like structures, we applied subtomogram averaging and three-dimensional (3D) classification analysis. Subtomogram averaging without external reference revealed a ∼29-nm-long and 6-nm-wide rod bridging the two membranes (Fig. 4*F* and *SI Appendix*, Figs. S6*A* and S7). An internal tunnel reflecting the hydrophobic groove could not be seen, but the length and diameter of the rod are in agreement with the structural prediction of VPS13C using AlphaFold, strongly suggesting that the rod is formed by VPS13C. Subtomogram averaging of VPS13C Δ1,235–1,748 revealed a ∼24-nm-long rod (Fig. 4*G*), which is also consistent with AlphaFold prediction (Fig. 4*I*). The presence of lipids or the insufficient resolution may obscure such a cavity. Lack of a density that could be assigned to Halo could be explained by the variable orientation of the Halo moiety, which was attached to a flexible loop of VPS13. Likewise, an arc reflecting the VAB domain as shown in low-resolution negative staining EM images of purified yeast VPS13 (16) could also not be detected, probably because of its variable orientation, as reported in that study. Interestingly, 3D classification analysis (*SI Appendix*, Fig. S6 *B–D*) revealed that for most classes the average density is less continuous with the ER membrane than with the endo/lysosome membrane (Fig. 4 *F*, *H*, and *J* and Movie S6). One possible explanation of this observation is that the N-terminal portion of VPS13C, which is in contact with the ER, is too flexible and therefore "averaged out." The other possibility is that the N-terminal region of VPS13C, which is anchored to the ER by VAP, is not always in direct contact with the ER bilayer (Fig. 4*J*). A flexible connection between VAP and VPS13C allowing a small gap is plausible: The domain of VAP that binds the FFAT motif (its MSP domain) is at the end of its cytosolic portion, which is ∼12 nm in length and comprises an unfolded region (37), while

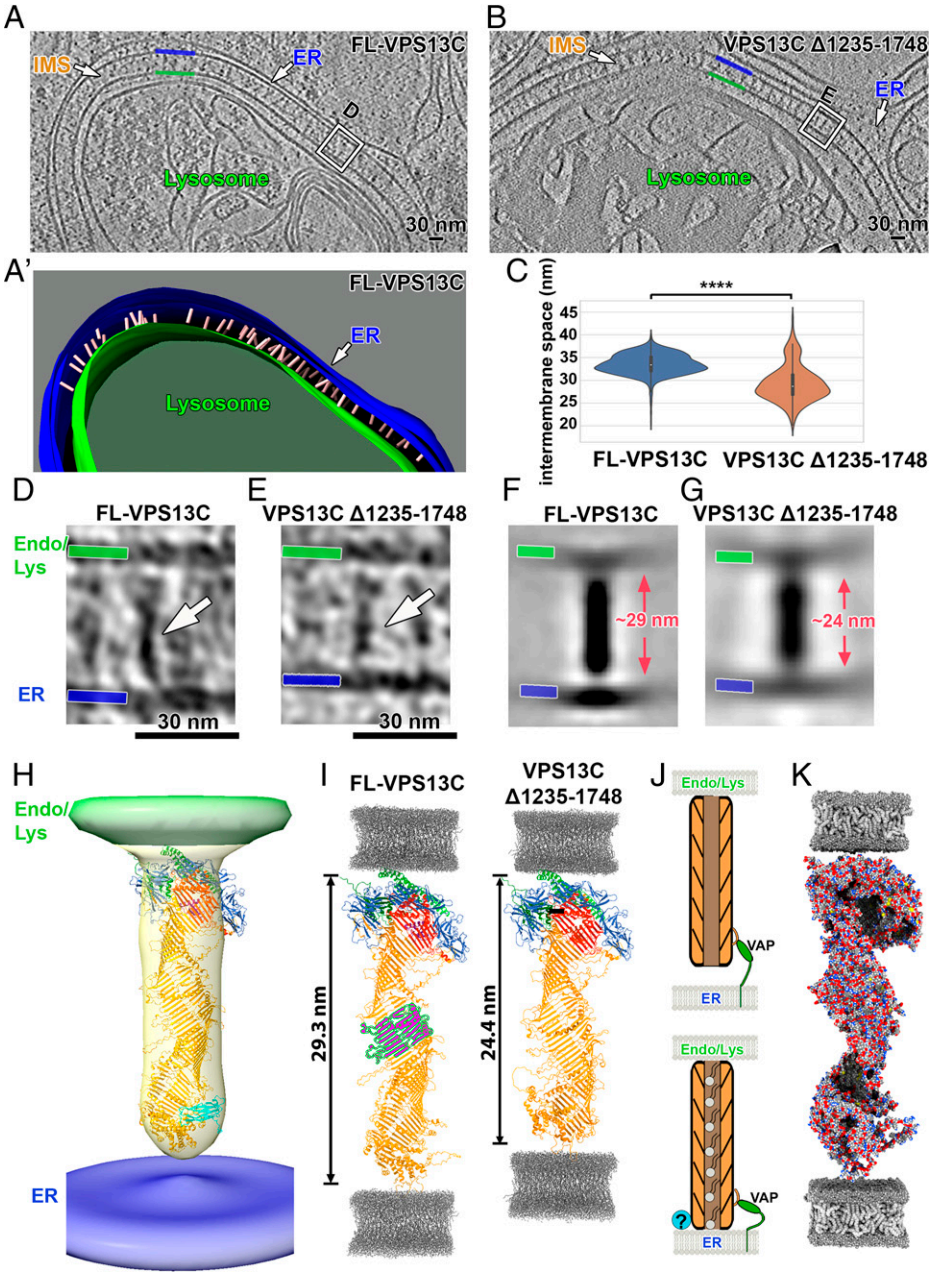

Fig. 4. Rod-like structures with the expected length of VPS13C bridge the membranes at contacts between the ER and lysosomes. (*A*) Cryotomographic slice (1 nm thick) showing abundant rod-shaped densities at ER–lysosome contacts in a HeLa cell overexpressing full-length VPS13C and VAP. Blue and green lines: ER and lysosome membrane, respectively. IMS: intermembrane space between the ER and the lysosome membrane. (*A'*) 3D segmentation view of panel *A*. Pink: VPS13C-like rod densities. (*B*) Cryotomographic slice (1 nm thick) showing shorter rod-shaped densities and narrower IMS relative to field *A*, at ER–lysosome contacts in a HeLa cell overexpressing a truncated VPS13C mutant (VPS13C Δ1,235–1,748) and VAP. (*C*) Violin plot showing the distribution of ER–lysosome intermembrane distances at contacts mediated by full-length VPS13C and VPS13C Δ1,235–1,748, respectively. ****$P < 0.0001$. (*D* and *E*) Enlarged views of the regions boxed in panel *A* (in a different tomographic slice) and panel *B*, respectively, showing rod-shaped densities bridging the ER membrane (blue) to the lysosome membrane (green). (*F* and *G*) Subtomogram-average density maps showing a 29-nm-long full-length VPS13C rod (panel *F*) and a 24-nm-long VPS13C Δ1,235–1,748 rod (panel *G*) bridging the two adjacent membranes. Rotational averaging was used to increase the signal-to-noise ratio. See *SI Appendix*, Fig. S6*A* for averages without applying rotational symmetry. (*H*) 3D view of panel *F*. The density corresponding to VPS13C is shown in light orange, fitted with the full-length VPS13C predicted structure from AlphaFold v2.0. The color scheme of predicted structure is consistent with the one shown in Fig. 1*A*. (*I*) Predicted structures of full-length VPS13C (*Left*) and VPS13C truncation mutant (Δ1,235–1,748) between two lipid bilayers. The fragment shown in magenta is removed from full-length VPS13C to generate the truncation mutant, which is ~5 nm shorter than the full-length protein. Gray: molecular dynamics simulation of lipid bilayer (58). (*J*) Cartoon depicting a putative dynamic association of VPS13C with the ER membrane due to the flexible linker region of VAP. (*K*) Proposed model of VPS13C arrangement at ER–endo/lysosome contacts. Surface representation of VPS13C predicted structure reveals a continuous hydrophobic groove (gray) along the protein. For clarity of presentation, some α-helices and disordered loops are not shown.

the VPS13C binding site for VAP (its FFAT motif) is localized on an unfolded loop of VPS13C at about 5 nm from the N-terminal end of the rod (Fig. 1 *B* and *E*). Altogether, our structural analysis supports a model according to which VPS13C functions as a bridge to channel lipids (Fig. 4*K*).

Discussion

Our study of VPS13C at ER–endo/lysosome contacts provides a view of a VPS13-ATG2 family protein in an intact cell and supports the hypothesis that these proteins function as bridges

that connect opposite membranes to allow lipid flux between them. The recently published AlphaFold algorithm has allowed us to correlate the predicted full-length structure of VPS13C with the densities obtained by cryo-EM, thus strengthening our conclusions. VPS13 proteins, which are very large, are expressed at low concentration in cells. Thus, in order to visualize with confidence VPS13C-dependent contacts, we had to overexpress VPS13C. Such overexpression may have helped force, by crowding, roughly parallel orientations of VPS13 perpendicular to the two membranes. When expressed at endogenous levels, VPS13 proteins may have more variable orientation and populate contacts with shorter distances between the two membranes if oriented obliquely. VPS13 proteins are very long. Their length may facilitate the formation of bridges when a VPS13 molecule anchored to one membrane explores the space for an appropriate partner membrane. In the case of other membrane tethers, including those that transport lipids by a shuttle mechanism, such a property may be achieved by unfolded flexible protein regions present in them.

An unexpected observation made possible by our 3D classification and subtomogram averaging analysis was that, in most classes, the N terminus of VPS13C appeared to be detached from ER (i.e., in a state that does not allow lipid extraction from the bilayer to enter the channel). We suggest that VPS13C may make at least two types of contacts with the ER. One is mediated by VAP, which functions as an adaptor to capture the N-terminal region of VPS13 via an interaction with its FFAT motif but does not force a direct contact of VPS13C with the ER bilayer because of the long and flexible linker region in VAP. The other one, supported by the occurrence of a subpopulation of VPS13C rods in direct contact with the ER membrane, could be a regulated, possibly low-affinity interaction of the highly conserved N-terminal chorein domain of VPS13C with some component (protein or lipid) of the ER membrane. Binding of VPS13C to VAP may facilitate the occurrence of this other interaction. We note that the chorein domain is the most conserved region in VPS13-ATG2 family proteins, leading to the speculation that such a motif is critically important for membrane binding and lipid extraction. Yet ATG2 and SHIP164, which have very similar chorein motifs (23, 28) but lack FFAT motifs for VAP binding, do not have an obvious localization throughout the ER even when overexpressed (24, 38). Likewise, VPS13A and VPS13C lose their ER association if their FFAT motif is deleted (17). Thus, VAP-independent ER interactions of VPS13C must be of low affinity, regulated, and transient. It was proposed that VMP1 and TMEM41, which have scramblase activity, represent binding sites in the ER for ATG2 (39). Along with this possibility, VMP21 was shown to function upstream of VPS13D in *Drosophila* (40). However, so far we have not detected an interaction of VPS13 with these proteins.

A dynamic association of VPS13 with the lipid bilayers may be a mechanism that contributes to a precise regulation of bulk lipid transfer to other membranes. Further elucidation of these mechanisms may not only advance fundamental knowledge about cell biology but also provide insight into how mutations of these proteins lead to neurodegenerative and neurodevelopmental disorders.

Methods

DNA Plasmids. A plasmid containing codon-optimized complementary DNA encoding full-length human VPS13C, with a Halo protein after amino acid residue 1914 (VPS13C^Halo), was generated by and purchased from GenScript Biotech. GFP-VAPB and PDZD8-EGFP were previously generated in our laboratory (35, 41). A deletion mutant of VPS13C lacking a.a. 1,235–1,748 (RRID: Addgene_187297) was generated as follows. First a C-terminal fragment of VPS13C^halo$_{1749–3753}$, including a Halo protein, was generated by PCR amplification from VPS13C^halo plasmid and ligated into pEGFP-C1 by InFusion Cloning using the EcoRI and KpnI sites. Then VPS13C^Halo (Δ1,235–1,748) construct was generated by PCR amplification from VPS13C^Halo plasmid and ligated into VPS13C^halo$_{1749–3753}$ plasmid by InFusion Cloning using the NheI and EcoRI sites.

Cell Culture and Transfection. HeLa and Cos-7 cells were cultured in Dulbecco's modified Eagle's medium (DMEM) (Thermo Fisher Scientific) supplemented with 10% fetal bovine serum (Thermo Fisher Scientific) and maintained at 37 °C, 5% CO_2 in a humidified incubator. For transfection, cells were seeded on 35-mm Petri dishes at a concentration of 50,000 cells per dish and transfected after 24 h with FuGene HD (Promega). The detailed protocol for cell culture and transfection was deposited in protocols.io (https://dx.doi.org/10.17504/protocols.io.ewov1n5p2gr2/v1).

Cell Culture on EM Grids. Preparation of EM grids for cell seeding was performed as previously described, with modifications (42). Four to six Quantifoil R2/4 Au-grids with carbon sides facing up were placed onto the center of a 35-mm glass-bottomed dish (MatTek, 0.15 mm in thickness and 2 mm in diameter). The carbon sides of the grids were glow discharged for 45 s at 15 mA in a plasma cleaner (PELCO easiGlow, Ted Pella, Redding, CA). The dish with grids was then sterilized in 5 mL of 70% ethanol for 10 min under ultraviolet light, washed with distilled water six times, and incubated with 1 mL of 0.1 mg/mL poly-D-lysine (Thermo Fisher Scientific) overnight in a 37 °C incubator. The grids were subsequently washed with distilled water six times and incubated with DMEM complete media overnight.

Right before seeding of cells, each grid was placed onto the center of a separate glass-bottomed dish (MatTek). Transfected cells were trypsinized, and 1,500 cells were seeded on each grid. The grid was incubated at 37 °C, 5% CO_2 for 10 min, and then 2 mL DMEM complete media was slowly added to each dish.

Live-Cell Fluorescence Microscopy. Cells transfected with VPS13C^halo and GFP-VAP were seeded on EM grids on glass-bottomed MatTek dishes 1 d before fluorescence imaging. Halo tag ligands JF549 were added to each dish at a final concentration of 200 nM. Cells were incubated with the dye for 1 h, rinsed three times, and then incubated in DMEM complete media for 1 h before imaging. Spinning-disk confocal imaging of the cells was performed with an Andor Dragonfly spinning-disk confocal microscope equipped with a plan apochromat objective (63×, 1.4 NA, oil) and a Zyla scientific CMOS camera at 37 °C and 5% CO_2. The grid was placed in an orientation with the "1" label at the top. Cells with bright VPS13C and VAP fluorescence were imaged, and their location relative to the center of the grid was recorded. The detailed protocol for cell culture on EM grids and fluorescence microscopy imaging was deposited in protocols.io (https://www.protocols.io/view/cell-culture-on-em-grids-and-fluorescence-microsco-b9hdr326).

Conventional Correlative Light and Electron Microscopy. For transmission correlative light electron microscopy (CLEM), Cos-7 cells were plated on 35-mm MatTek dish (P35G-1.5-14-CGRD) and transfected with VPS13C^Halo, EGFP-VAP-B, PDZD8-EGFP, and mCherry-Rab7a (RRID:Addgene_61804) constructs. Cells were prefixed in 4% paraformaldehyde + 0.25% glutaraldehyde in Live Cell Imaging Buffer (Life Technologies), then washed before fluorescence light microscopy imaging. Regions of interest were selected, and their coordinates on the dish were identified via phase contrast. Cells were further fixed with 2.5% glutaraldehyde in 0.1 M sodium cacodylate buffer, postfixed in 2% OsO_4 and 1.5% K4Fe(CN)6 (Sigma-Aldrich) in 0.1 M sodium cacodylate buffer, en bloc stained with 2% aqueous uranyl acetate, dehydrated, and embedded in Embed 812. Cells of interest were relocated based on the prerecorded coordinates. Ultrathin sections (50–60 nm) were observed in a Talos L 120C TEM microscope at 80 kV, and images were taken with Velox software and a 4k × 4K Ceta CMOS Camera (Thermo Fisher Scientific). The detailed protocol for 2D TEM CLEM was deposited in protocols.io (https://www.protocols.io/view/2d-tem-clem-correlative-light-microscopy-and-elect-b5wnq7de).

For correlative light microscopy and FIB-SEM, VPS13C^Halo and PDZD8-EGFP were coexpressed in Cos7 cells and processed as above with the exception that except fluorescence light microscopy, imaging was carried out in live mode without the prefixation with paraformaldehyde. Epon blocks were glued onto the scanning electron microscope mounting aluminum stub. Next, platinum en

bloc coating (20–25 nm thick) of the sample surface was applied with the sputter coater (Ted Pella, Inc., Redding, CA). Samples were FIB-SEM imaged in a Crossbeam 550 FIB-SEM workstation operating under SmartSEM (Carl Zeiss Microscopy GmbH, Oberkochen, Germany) and Atlas 5 engine (Fibics Incorporated, Ottawa, Canada). The imaging resolution was set at 7 nm/pixel in the *x*, *y* axes, with milling being performed at 7 nm/step along the *z* axis to achieve an isotropic resolution of 7 nm/voxel. Images were aligned and exported in Atlas 5 (Fibics Incorporated, Ottawa, Canada), further processed, and analyzed with DragonFly Pro software (Object Research Systems Inc., Montreal, Canada). Except when noted, all reagents were from EMS (Electron Microscopy Sciences, Hatfield, PA). The detailed protocol for 3D FIB-SEM CLEM was deposited in protocols.io (https://www.protocols.io/view/3d-fibsem-clem-b5wsq7ee).

Plunge Freezing. Dishes with grids were taken out of the incubator, and the medium of each dish was replaced with 1 mL of live-cell imaging solution (Life Technologies) to maintain physiological pH. Plunge freezing was performed with Vitrobot Mk IV (Thermo, Waltham, MA). The Vitrobot was set to 37 °C, 100% humidity. The grid seeded with cells was held with a Vitrobot tweezer, immersed in a live-cell imaging solution with 3–5% glycerol for 1 min, and then mounted onto the Vitrobot and blotted once in the Vitrobot chamber (blot force: 10, blot time: 10 s). To ensure that cells on the grids were not too dry, the side of the chamber facing the carbon side of the grid (where cells are located) was covered with two layers of Parafilm, while the side facing the gold side of the grid was covered with two layers of blotting paper (Whatman). The grid was then plunged into a liquid ethane–propane mixture (4:6 ratio). The detailed protocol for plunge freezing was deposited in protocols.io (https://www.protocols.io/view/plunge-freezing-b9fer3je).

Cryo-Focused Ion Beam Milling. Micromachining of frozen hydrated cells was performed in FEI Aquilos1 and Aquilos2 FIB/SEM systems, operated at a temperature below –180 °C. Grids were imaged by SEM imaging (5 kV, 21 pA) to check the quality of the sample. Samples were sputter coated with a platinum metal layer for 15 s. Then a gas injection system deposition of organo-platinum was applied for 10–15 s. Cryo-lamellae were milled in several steps. A 9-μm-wide and 3-μm-thick cryo-lamella was first generated with the ion beam set to 30 kV and ∼500 pA. The ion beam current was then decreased gradually until the cryo-lamella reached a nominal thickness of 500 nm (ion beam set to 50 pA). After the thinning of all cryo-lamellae, each cryo-lamella was polished to a nominal thickness of ∼100–150 nm (ion beam set to 10 or 30 pA). An SEM image of each cryo-lamella was taken at 5 kV, 30 pA, 1 μs dwell time. The polishing step was completed within an hour to minimize contamination. A thin platinum metal layer was then applied (4–5 s sputter coating) to increase the electrical conductivity of the cryo-lamella surface if phase plates were used during the following TEM imaging. The detailed protocol for cryo-FIB was deposited in protocols.io (https://www.protocols.io/view/cryo-focused-ion-beam-milling-b9ewr3fe).

Cryo-Electron Tomography Data Acquisition. Cryo-lamella grids were visualized in a Titan Krios electron microscope (Thermo Fisher Scientific) equipped with a field emission gun, a GIF Quantum LS postcolumn energy filter (Gatan), and a K3 Summit direct electron detector (Gatan). The electron microscope was operated at 300 kV in nanoprobe mode at magnification 26,000× (pixel size of 3.3 Å at the specimen level). Cryo-ET tilt series with a dose-symmetric acquisition scheme (43) were acquired at a target defocus of –6 μm without Volta phase plate (VPP) or –1 μm with VPP in SerialEM (44, 45). The K3 detector was operated in counting mode, and 10 sequentially acquired 0.1-s frames were combined. The tilt range was typically between ±50° and ±60°, with increments of 3°, and the total electron dose was about 80 e/Å^2. Imaging details are shown in *SI Appendix*, Table S1.

Cryo-ET Data Alignment and Reconstruction. The frames of each tilt series micrograph were aligned in MotionCor2 (version 1.4.0, https://emcore.ucsf.edu/ucsf-software, RRID:SCR_016499) (46). For defocus-contrast micrographs, contrast transfer function correction was performed in Gctf (version 1.18, https://www2.mrc-lmb.cam.ac.uk/research/locally-developed-software/zhang-software, RRID:SCR_016500) (47). A script written by Yan Rui from the HHMI Janelia CryoEM Facility was used to reorder and combine tilt series micrographs. Alignment of the tilt series and tomographic reconstructions was performed in Etomo, which is part of the IMOD package (version 4.11.12, https://bio3d.colorado.edu/imod, RRID:SCR_003297) (48). Fiducial tracking was performed with 5- to 10-nm gold-bead-like deposits on the lamellae. Tomograms were reconstructed via the weighted back-projection and simultaneous iterative reconstruction technique. Tomograms were 4×-binned for subsequent analysis. For figure presentation of defocus-contrast tomograms, either a nonlinear anisotropic diffusion filter (48) or a deconvolution filter [https://github.com/dtegunov/tom_deconv (49)] was applied to increase contrast. Segmentation of ER, endo/lysosome membranes, and microtubules was done in IMOD (48). Segmentation of ribosomes was done in EMAN2 (version 2.91, https://blake.bcm.edu/emanwiki/EMAN2/Install/BinaryInstallAnaconda/2.91, RRID:SCR_016867) (50). More details of image analysis and the datasets used in this article are shown in *SI Appendix*, Tables S1 and S2, respectively. The detailed protocol for cryo-ET data collection and reconstruction was deposited in protocols.io (https://www.protocols.io/view/tilt-series-collection-and-reconstruction-for-cryo-b9eyr3fw).

Subtomogram Averaging and 3D Classification. Rod-shaped VPS13C-like densities were manually selected (full-length VPS13C, 576 in total; VPS13C Δ1,235–1,748, 110 in total) from 4× binned VPP-contrast or defocus-contrast tomograms in IMOD, with the first point on the tip of the VPS13C rod close to ER and the second point on the tip at the opposite side, next to the endo/lysosome. From the tomograms, 4× binned subtomograms were extracted at the centers of the rod-like densities. The orientations (two Euler angles) of the rod-like densities were estimated based on two membrane contact points. Subtomogram averaging package i3 (version 0.9.9.3, https://www.electrontomography.org, RRID:SCR_017296) was used for 3D alignment and classification (51, 52). A global average of all of the extracted subtomograms without alignment was first performed after the two Euler angles previously estimated were applied. This global average served as an initial reference for translational and rotational alignment. To avoid flipping the orientation of rods during alignment, we constrained rotational range by setting the angular range between –30° and 30°. Multivariate statistical analysis was then performed with a mask around the entire rod or the N-terminal portion of the rod. Hierarchical ascendant classification was subsequently performed with manually picked eigenfactors. Class averages that resemble a rod were selected and aligned to each other to generate a new global average with resolution estimated by Fourier shell correlation coefficients (FSCs). The global average served as a new reference for the next iteration. The alignment and classification were performed iteratively until there was no more improvement of the average as estimated by FSCs. These FSCs were calculated in the i3 software package and plotted in Excel. The remapping of rods to the original tomogram was done with the scripts i3_to_RELION.py (https://github.com/scai20/i3, DOI: 10.5281/zenodo.6618390) and ot_remap.py (https://github.com/anaphaze/ot-tools) and visualized in UCSF Chimera (version 1.13, https://www.rbvi.ucsf.edu/chimera, RRID:SCR_004097) (53). Rigid-body fitting of AlphaFold-predicted structure into the averaged density map was done in UCSF ChimeraX_Daily (version 1.4.dev202204302327, https://www.cgl.ucsf.edu/chimerax, RRID:SCR_015872) (54). The detailed protocol for subtomogram averaging and classification was deposited in protocols.io (https://dx.doi.org/10.17504/protocols.io.81wgb6qqqlpk/v1).

Measuring Distances Between Membranes. Segmentation of ER and endo/lysosome membranes in close contact with each other was done in IMOD (48). The coordinates were subsequently extracted. The nearest-neighbor distance between multiple points on the ER membrane and multiple points on the endo/lysosome membrane within the segmented area was calculated, and the distribution was plotted with a custom Python (RRID:SCR_008394) script (https://github.com/scai20/Intermembrane-space, DOI:10.5281/zenodo.6618374). A violin plot was generated with the Python data visualization library Seaborn (version 0.11.2, https://seaborn.pydata.org/index.html, RRID:SCR_018132) (55). The detailed protocol for measuring intermembrane spacing was deposited in protocols.io (https://www.protocols.io/view/determine-inter-membrane-spacing-b9hrr356).

AlphaFold Structure Prediction. Structural predictions of segments of full-length human VPS13C (a.a. 1–1,860, 1,201–2,340, and 1,801–3,753), VPS13C truncation mutant Δ1,235–1,748 (a.a. 1–1,762 and 1,277–3,240) were generated with AlphaFold v2.0 and v2.1.1 (https://github.com/deepmind/alphafold) (29) on the Yale Farnam high-performance computer cluster. Segments were joined by UCSF ChimeraX (54). Specifically, the segments with overlapping regions were aligned with the "mmaker" command. Then, the overlapping regions from adjacent fragments were deleted with the "delete" command. At the connection point, a carbon–nitrogen bond was formed with the "build join peptide" command to connect two amino acid residues from two segments. The detailed protocol for structure

prediction of VPS13C was deposited in protocols.io (https://www.protocols.io/view/structural-prediction-of-vps13c-with-alphafold2-b9hnr35e).

AlphaFold-Multimer (30) was used to predict the interaction between VPS13C N terminus and VAP.

Data Availability. Subtomogram-average density maps showing a full-length VPS13C rod and a VPS13C Δ1,235–1,748 rod bridging the two adjacent membranes have been deposited at EMDB as entry EMD-26247 (56). The raw cryo-ET tilt series and reconstructed tomograms presented in Figs. 3 and 4 and *SI Appendix*, Fig. S2 have been deposited in EMPIAR (57) under entry EMPIAR-10962.

Human VPS13C structure predicted by AlphaFold is available in https://doi.org/10.5281/zenodo.6803512 (59) and in https://modelarchive.org/doi/10.5452/ma-zbd1a.

All study data are included in the article and/or supporting information.

ACKNOWLEDGMENTS. We thank Marianna Leonzino, Xia Li, and Lu Gan (National University of Singapore) for advice and discussion and Karin Reinisch for critical reading of the manuscript. We acknowledge the support of the cryo-EM facilities of the Yale West Campus, the Yale Center for Cell Imaging of the Yale Medical School, and the HHMI Janelia Research Campus. This work was supported in part by grants from the NIH (DA018343, NS36251 to P.D.C. and AI152421 to J.L.) and by the Kavli Institute for Neuroscience, the Parkinson's Foundation, the Chan Zuckerberg Initiative DAF, an advised fund of Silicon Valley Community Foundation, and Aligning Science Across Parkinson's grant (ASAP-000580) through the Michael J. Fox Foundation for Parkinson's Research to P.D.C. For the purpose of open access, the authors have applied a CC BY public copyright license to all Author Accepted Manuscripts arising from this submission. S.C. was supported by a fellowship from the Parkinson's Foundation. P.D.C. serves on the scientific advisory board of Casma Therapeutics.

1. H. Wu, P. Carvalho, G. K. Voeltz, Here, there, and everywhere: The importance of ER membrane contact sites. *Science* **361**, eaan5835 (2018).
2. T. Balla, Y. J. Kim, A. Alvarez-Prats, J. Pemberton, Lipid dynamics at contact sites between the endoplasmic reticulum and other organelles. *Annu. Rev. Cell Dev. Biol.* **35**, 85–109 (2019).
3. K. M. Reinisch, W. A. Prinz, Mechanisms of nonvesicular lipid transport. *J. Cell Biol.* **220**, e202012058 (2021).
4. Y. Saheki, P. De Camilli, Endoplasmic reticulum-plasma membrane contact sites. *Annu. Rev. Biochem.* **86**, 659–684 (2017).
5. L. H. Wong, A. T. Gatta, T. P. Levine, Lipid transfer proteins: The lipid commute via shuttles, bridges and tubes. *Nat. Rev. Mol. Cell Biol.* **20**, 85–101 (2019).
6. M. Leonzino, K. M. Reinisch, P. De Camilli, Insights into VPS13 properties and function reveal a new mechanism of eukaryotic lipid transport. *Biochim. Biophys. Acta Mol. Cell Biol. Lipids* **1866**, 159003 (2021).
7. J. H. Rothman, T. H. Stevens, Protein sorting in yeast: Mutants defective in vacuole biogenesis mislocalize vacuolar proteins into the late secretory pathway. *Cell* **47**, 1041–1051 (1986).
8. V. A. Bankaitis, L. M. Johnson, S. D. Emr, Isolation of yeast mutants defective in protein targeting to the vacuole. *Proc. Natl. Acad. Sci. U.S.A.* **83**, 9075–9079 (1986).
9. J. H. Brickner, R. S. Fuller, SOI1 encodes a novel, conserved protein that promotes TGN-endosomal cycling of Kex2p and other membrane proteins by modulating the function of two TGN localization signals. *J. Cell Biol.* **139**, 23–36 (1997).
10. A. B. Lang, A. T. John Peter, P. Walter, B. Kornmann, ER-mitochondrial junctions can be bypassed by dominant mutations in the endosomal protein Vps13. *J. Cell Biol.* **210**, 883–890 (2015).
11. J. S. Park *et al.*, Yeast Vps13 promotes mitochondrial function and is localized at membrane contact sites. *Mol. Biol. Cell* **27**, 2435–2449 (2016).
12. L. Rampoldi *et al.*, A conserved sorting-associated protein is mutant in chorea-acanthocytosis. *Nat. Genet.* **28**, 119–120 (2001).
13. J. Kolehmainen *et al.*, Cohen syndrome is caused by mutations in a novel gene, COH1, encoding a transmembrane protein with a presumed role in vesicle-mediated sorting and intracellular protein transport. *Am. J. Hum. Genet.* **72**, 1359–1369 (2003).
14. S. Lesage *et al.*; French Parkinson's Disease Genetics Study (PDG); International Parkinson's Disease Genomics Consortium (IPDGC), Loss of VPS13C function in autosomal-recessive parkinsonism causes mitochondrial dysfunction and increases PINK1/Parkin-dependent mitophagy. *Am. J. Hum. Genet.* **98**, 500–513 (2016).
15. E. Seong *et al.*, Mutations in VPS13D lead to a new recessive ataxia with spasticity and mitochondrial defects. *Ann. Neurol.* **83**, 1075–1088 (2018).
16. M. De *et al.*, The Vps13p-Cdc31p complex is directly required for TGN late endosome transport and TGN homotypic fusion. *J. Cell Biol.* **216**, 425–439 (2017).
17. N. Kumar *et al.*, VPS13A and VPS13C are lipid transport proteins differentially localized at ER contact sites. *J. Cell Biol.* **217**, 3625–3639 (2018).
18. B. D. M. Bean *et al.*, Competitive organelle-specific adaptors recruit Vps13 to membrane contact sites. *J. Cell Biol.* **217**, 3593–3607 (2018).
19. P. Li, J. A. Lees, C. P. Lusk, K. M. Reinisch, Cryo-EM reconstruction of a VPS13 fragment reveals a long groove to channel lipids between membranes. *J. Cell Biol.* **219**, e202001161 (2020).
20. A. Guillen-Samander *et al.*, VPS13D bridges the ER to mitochondria and peroxisomes via Miro. *J. Cell Biol.* **220**, e202010004 (2021). Correction in: *J. Cell Biol.* **220**, e20201000405052021c (2021).
21. W. Hancock-Cerutti *et al.*, ER-lysosome lipid transfer protein VPS13C/PARK23 prevents aberrant mtDNA-dependent STING signaling. *J Cell Biol* 221 (2022).
22. A. T. John Peter *et al.*, Vps13-Mcp1 interact at vacuole-mitochondria interfaces and bypass ER-mitochondria contact sites. *J. Cell Biol.* **216**, 3219–3229 (2017).
23. T. Osawa *et al.*, Atg2 mediates direct lipid transfer between membranes for autophagosome formation. *Nat. Struct. Mol. Biol.* **26**, 281–288 (2019).
24. D. P. Valverde *et al.*, ATG2 transports lipids to promote autophagosome biogenesis. *J. Cell Biol.* **218**, 1787–1798 (2019).
25. M. Beck, W. Baumeister, Cryo-electron tomography: Can it reveal the molecular sociology of cells in atomic detail? *Trends Cell Biol.* **26**, 825–837 (2016).
26. J. Collado *et al.*, Tricalbin-mediated contact sites control ER curvature to maintain plasma membrane integrity. *Dev. Cell* **51**, 476–487.e7 (2019).
27. P. C. Hoffmann *et al.*, Tricalbins contribute to cellular lipid flux and form curved ER-PM contacts that are bridged by rod-shaped structures. *Dev. Cell* **51**, 488–502.e8 (2019).
28. B. Ugur, W. Hancock-Cerutti, M. Leonzino, P. De Camilli, Role of VPS13, a protein with similarity to ATG2, in physiology and disease. *Curr. Opin. Genet. Dev.* **65**, 61–68 (2020).
29. J. Jumper *et al.*, Highly accurate protein structure prediction with AlphaFold. *Nature* **596**, 583–589 (2021).
30. R. Evans *et al.*, Protein complex prediction with AlphaFold-Multimer. *BioRxiv* [Preprint] (2021). https://www.biorxiv.org/content/10.1101/2021.10.04.463034v2.
31. L. Aravind, The WWE domain: A common interaction module in protein ubiquitination and ADP ribosylation. *Trends Biochem. Sci.* **26**, 273–275 (2001).
32. J. Adlakha, Z. Hong, P. Li, K. M. Reinisch, Structural and biochemical insights into lipid transport by VPS13 proteins. *J. Cell Biol.* **221**, e202202030 (2022).
33. Y. Wu *et al.*, Contacts between the endoplasmic reticulum and other membranes in neurons. *Proc. Natl. Acad. Sci. U.S.A.* **114**, E4859–E4867 (2017).
34. L. Orci *et al.*, From the Cover: STIM1-induced precortical and cortical subdomains of the endoplasmic reticulum. *Proc. Natl. Acad. Sci. U.S.A.* **106**, 19358–19362 (2009).
35. A. Guillén-Samander, X. Bian, P. De Camilli, PDZD8 mediates a Rab7-dependent interaction of the ER with late endosomes and lysosomes. *Proc. Natl. Acad. Sci. U.S.A.* **116**, 22619–22623 (2019).
36. F. Alpy *et al.*, STARD3 or STARD3NL and VAP form a novel molecular tether between late endosomes and the ER. *J. Cell Sci.* **126**, 5500–5512 (2013).
37. E. de la Mora *et al.*, Nanoscale architecture of a VAP-A-OSBP tethering complex at membrane contact sites. *Nat. Commun.* **12**, 3459 (2021).
38. M. G. Hanna, P. H. Suen, Y. Wu, K. M. Reinisch, P. De Camilli, SHIP164 is a chorein motif lipid transfer protein that controls endosome-Golgi membrane traffic. *J Cell Biol.* **221** (2022).
39. A. Ghanbarpour, D. P. Valverde, T. J. Melia, K. M. Reinisch, A model for a partnership of lipid transfer proteins and scramblases in membrane expansion and organelle biogenesis. *Proc. Natl. Acad. Sci. U.S.A.* **118**, e2101562118 (2021).
40. J. L. Shen *et al.*, Vmp1, Vps13D, and Marf/Mfn2 function in a conserved pathway to regulate mitochondria and ER contact in development and disease. *Curr. Biol.* **31**, 3028–3039.e7 (2021).
41. R. Dong *et al.*, Endosome-ER contacts control actin nucleation and retromer function through VAP-dependent regulation of PI4P. *Cell* **166**, 408–423 (2016).
42. X. Li *et al.*, Symmetrical organization of proteins under docked synaptic vesicles. *FEBS Lett.* **593**, 144–153 (2019).
43. W. J. Hagen, W. Wan, J. A. Briggs, Implementation of a cryo-electron tomography tilt-scheme optimized for high resolution subtomogram averaging. *Journal of Structural Biology* **197**, 191–198 (2017).
44. D. N. Mastronarde, E. M. Serial, A program for automated tilt series acquisition on Tecnai microscopes using prediction of specimen position. *Microsc. Microanal.* **9**, 1182–1183 (2003).
45. R. Danev, B. Buijsse, M. Khoshouei, J. M. Plitzko, W. Baumeister, Volta potential phase plate for in-focus phase contrast transmission electron microscopy. *Proc. Natl. Acad. Sci. U.S.A.* **111**, 15635–15640 (2014).
46. S. Q. Zheng *et al.*, MotionCor2: Anisotropic correction of beam-induced motion for improved cryo-electron microscopy. *Nat. Methods* **14**, 331–332 (2017).
47. K. Zhang, Gctf: Real-time CTF determination and correction. *J. Struct. Biol.* **193**, 1–12 (2016).
48. J. R. Kremer, D. N. Mastronarde, J. R. McIntosh, Computer visualization of three-dimensional image data using IMOD. *J. Struct. Biol.* **116**, 71–76 (1996).
49. D. Tegunov, P. Cramer, Real-time cryo-electron microscopy data preprocessing with Warp. *Nat. Methods* **16**, 1146–1152 (2019).
50. G. Tang *et al.*, EMAN2: An extensible image processing suite for electron microscopy. *J. Struct. Biol.* **157**, 38–46 (2007).
51. H. Winkler, 3D reconstruction and processing of volumetric data in cryo-electron tomography. *J. Struct. Biol.* **157**, 126–137 (2007).
52. H. Winkler *et al.*, Tomographic subvolume alignment and subvolume classification applied to myosin V and SIV envelope spikes. *J. Struct. Biol.* **165**, 64–77 (2009).
53. E. F. Pettersen *et al.*, UCSF Chimera–A visualization system for exploratory research and analysis. *J. Comput. Chem.* **25**, 1605–1612 (2004).
54. E. F. Pettersen *et al.*, UCSF ChimeraX: Structure visualization for researchers, educators, and developers. *Protein Sci.* **30**, 70–82 (2021).
55. M. L. Waskom, Seaborn: Statistical data visualization. *J. Open Source Softw.* **6**, 3021 (2021).
56. S. Cai, P. De Camilli, In situ architecture of VPS13C. Electron Microscopy Data Bank. https://www.ebi.ac.uk/emdb/EMD-26247. Deposited 2 February 2022.
57. A. Iudin, P. K. Korir, J. Salavert-Torres, G. J. Kleywegt, A. Patwardhan, EMPIAR: A public archive for raw electron microscopy image data. *Nat. Methods* **13**, 387–388 (2016).
58. H. Heller, M. Schaefer, K. Schulten, Molecular dynamics simulation of a bilayer of 200 lipids in the gel and in the liquid crystal phase. *J. Phys. Chem.* **97**, 8343–8360 (1993).
59. S. Cai *et al.*, In situ architecture of the lipid transport protein VPS13C at ER–lysosome membrane contacts. Zenodo. 10.5281/zenodo.6803512. Accessed 6 July 2022.